

# Three-dimensional spin-orbit coupled Fermi gases: Fulde-Ferrell pairing, Majorana fermions, Weyl fermions and gapless topological superfluidity

Xia-Ji Liu<sup>1</sup>, Hui Hu<sup>1</sup>, and Han Pu<sup>2\*</sup>

<sup>1</sup>Centre for Quantum and Optical Science, Swinburne University of Technology, Melbourne 3122, Australia and  
<sup>2</sup>Department of Physics and Astronomy, and Rice Quantum Institute, Rice University, Houston, TX 77251, USA

(Dated: June 15, 2021)

We theoretically investigate a three-dimensional Fermi gas with Rashba spin-orbit coupling in the presence of both out-of-plane and in-plane Zeeman fields. We show that, driven by a sufficiently large Zeeman field, either out-of-plane or in-plane, the superfluid phase of this system exhibits a number of interesting features, including inhomogeneous Fulde-Ferrell pairing, gapped or gapless topological order and exotic quasi-particle excitations known as Weyl fermions that have linear energy dispersions in momentum space (i.e., massless Dirac fermions). The topological superfluid phase can have either four or two topologically protected Weyl nodes. We present the phase diagrams at both zero and finite temperatures and discuss the possibility of their observation in an atomic Fermi gas with synthetic spin-orbit coupling. In this context, topological superfluid phases with an imperfect Rashba spin-orbit coupling are also studied.

PACS numbers: 05.30.Fk, 03.75.Hh, 03.75.Ss, 67.85.-d

## I. INTRODUCTION

Quantum simulations of intriguing many-body problems with ultracold atoms have now become a paradigm in different fields of physics [1]. The major advantage of ultracold atoms is their unprecedented controllability in tuning interactions, dimensionality, populations and species of atoms, which constitutes an ideal toolbox for understanding the consequence of strong interactions [2]. Most recently, a new tool - a synthetic non-Abelian gauge field or spin-orbit coupling - was added to the toolbox [3]. In condensed matter physics, it is well known that spin-orbit coupling plays a key role in new-generation solid-state materials such as topological insulators [4, 5], quantum spin Hall systems [6] and non-centrosymmetric superconductors [7]. In this respect, recent realizations of synthetic spin-orbit coupling in ultracold atoms open an entirely new direction to quantum simulate and characterize these new-generation materials, without the need to overcome the intrinsic complexity in compositions and interactions, which is often encountered in solid-state systems.

Indeed, over the past few years, there have been a tremendous amount of theoretical works along this direction [8–49], triggered by the demonstration of a particular spin-orbit coupling in ultracold atomic Fermi gases by the two-photon Raman technique, which has an equal-weight superposition of Rashba and Dresselhaus spin-orbit couplings [50–53]. At the early stage, the possibility of observing a peculiar two-body bound state and the related anisotropic superfluid induced by Rashba spin-orbit coupling was discussed [11, 13, 14]. In the presence of out-of-plane Zeeman field, the routine to a topological superfluid and Majorana fermions in two dimen-

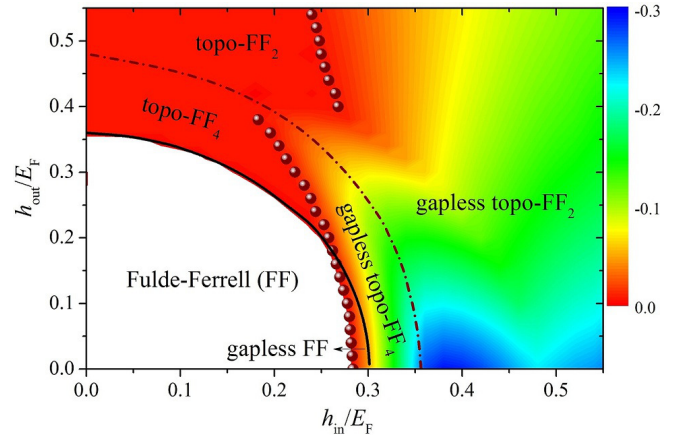


FIG. 1: (Color online) Zero temperature phase diagram of a 3D Rashba spin-orbit coupled Fermi gas on the plane of in-plane and out-of-plane Zeeman fields, with a spin-orbit coupling strength  $\lambda = E_F/k_F$  and an interaction strength  $1/(k_F a_s) = -0.5$ . The color map shows the lowest energy in the lower particle branch, in units of  $E_F$ . There are various superfluid phases, as described in detail in the text. The solid line show the topological phase transition. While the dot-dashed line indicates the transition within the two types of topological superfluids, which have four or two Weyl nodes/loops, respectively. The solid circles are the boundary where superfluid becomes gapless, apart from the Weyl nodes.

sions [12, 17, 21, 26, 54] or to a Weyl superfluid in three dimensions [15, 34, 55] - which has exotic quasiparticles with linear energy dispersion in momentum space - was addressed. Later on, it was realized that unconventional Fulde-Ferrell pairing could be significantly enhanced by spin-orbit coupling in combination with in-plane Zeeman field due to the distorted Fermi surface [27–33, 35, 41, 42]. As a result, spin-orbit coupled Fermi gases provide an ideal candidate to investigate the long-sought Fulde-Ferrell superfluidity or superconductivity

\*Electronic address: hpu@rice.edu

[56], which is yet to be unambiguously confirmed in solid-state systems. Very recently, it was shown that the Fulde-Ferrell pairing may coexist with the topological order, leading to the predictions of topological Fulde-Ferrell superfluids [37–40, 47], including a brand-new quantum matter of *gapless* topological superfluid that has no analogies in solid-state systems [43, 45, 49].

In this work, by using a spin-orbit coupled Fermi gas in three dimensions with both in-plane and out-of-plane Zeeman fields as a prototype, we show that the above-mentioned concepts in unconventional superfluid phases, including Fulde-Ferrell pairings, Majorana fermions, Weyl fermions and topological superfluidity, can be examined and demonstrated in near-future experiments. Our main result is summarized in Fig. 1, which displays a very rich phase diagram at zero temperature and at an interaction parameter  $1/(k_F a_s) = -0.5$  and a spin-orbit coupling strength  $\lambda = E_F/k_F$ , where  $k_F$  and  $E_F = \hbar^2 k_F^2/(2m)$  are respectively the Fermi wavevector and Fermi energy, and  $a_s$  is the  $s$ -wave scattering length. By tuning the in-plane and out-of-plane Zeeman fields, the Fermi system can support various intriguing unconventional superfluid phases: the Fulde-Ferrell superfluid (FF), topologically non-trivial Fulde-Ferrell superfluid with four (topo-FF<sub>4</sub>) or two Weyl nodes (topo-FF<sub>2</sub>), gapless Fulde-Ferrell superfluid (gapless FF), and gapless topologically non-trivial Fulde-Ferrell superfluid with four (gapless topo-FF<sub>4</sub>) or two Weyl nodes/loops (gapless topo-FF<sub>2</sub>). The purpose of this work is to discuss in detail the emergence of these interesting superfluid phases, their thermodynamic stability and their dependence on the form of spin-orbit coupling.

We note that the same Fermi system has been considered earlier by Xu *et al.* with the focus on the anisotropic Weyl fermions due to an in-plane Zeeman field [44]. Our results differ theirs in several ways: (1) We clarify that the in-plane Zeeman field itself can drive a topological phase transition and lead to a gapless topological superfluid; (2) In the topological phases, a Fulde-Ferrell superfluid, either gapped or gapless, can be further classified according to the number of Weyl nodes (in the gapped area) or Weyl loops (in the gapless region). With increasing Zeeman field, a topologically trivial phase first becomes a topologically non-trivial phase with four Weyl nodes/loops and then turns into the one with two Weyl nodes/loops when the Zeeman field is sufficiently large; Majorana surface states in different superfluid phases are discussed. (3) Various finite-temperature phase diagrams are presented, which are useful for future experiments that have to be carried out at non-zero temperatures; (4) We consider alternative form of spin-orbit coupling away from the Rashba limit and show different intriguing topological phases do not depend critically on the type of spin-orbit coupling.

On the other hand, we also note that our theoretical investigations are based on mean-field theory. The beyond mean-field effect has been recently considered by Zheng and co-workers [48], by using a pseudogap approximation

for pair fluctuations.

Our paper is organized as follows. In the next section, we introduce the mean-field theoretical framework. In Sec. III, we discuss in detail the conditions for different unconventional superfluid phases, their energy spectrum and the surface states when a hard-wall potential is imposed at the (opposite) two boundaries. Finite temperature phase diagrams at different Zeeman fields are constructed. We also investigate how the zero-temperature phase diagram is affected by the form of spin-orbit coupling. Finally, Sec. IV is devoted to the conclusions and outlooks.

## II. THEORETICAL FRAMEWORK

We consider a three-dimensional (3D) spin-1/2 Fermi gas of <sup>6</sup>Li or <sup>40</sup>K atoms near broad Feshbach resonances with two-dimensional (2D) spin-orbit coupling  $\lambda_z \hat{k}_z \sigma_z + \lambda_x \hat{k}_x \sigma_x$  in the presence of an in-plane Zeeman field  $h_{\text{in}} \sigma_z$  along the  $z$ -direction (i.e., on the  $z$ - $x$  plane of spin-orbit coupling) and an out-of-plane Zeeman field  $h_{\text{out}} \sigma_y$  along the  $y$ -direction perpendicular to the plane of spin-orbit coupling [33, 44]. Here,  $\hat{k}_x \equiv -i\partial_x$ ,  $\hat{k}_y \equiv -i\partial_y$  and  $\hat{k}_z \equiv -i\partial_z$  are the momentum operators, and  $\sigma_x$ ,  $\sigma_y$  and  $\sigma_z$  are the Pauli matrices. We assume a general form of 2D spin-orbit coupling with  $\lambda_z = \lambda \cos \theta$  and  $\lambda_x = \lambda \sin \theta$ , where the case of  $\theta = \pi/4$  corresponds to the Rashba spin-orbit coupling. The system can be described by the model Hamiltonian,

$$H = \int d\mathbf{x} [\mathcal{H}_0(\mathbf{x}) + \mathcal{H}_{\text{int}}(\mathbf{x})], \quad (1)$$

where  $\mathcal{H}_0(\mathbf{x})$  is the single-particle (density) Hamiltonian

$$\mathcal{H}_0 = \begin{bmatrix} \psi_{\uparrow}^{\dagger} & \psi_{\downarrow}^{\dagger} \end{bmatrix} \begin{bmatrix} \hat{\xi}_{\mathbf{k}} + \lambda_z \hat{k}_z + h_{\text{in}} & \lambda_x \hat{k}_x - i h_{\text{out}} \\ \lambda_x \hat{k}_x + i h_{\text{out}} & \hat{\xi}_{\mathbf{k}} - \lambda_z \hat{k}_z - h_{\text{in}} \end{bmatrix} \begin{bmatrix} \psi_{\uparrow} \\ \psi_{\downarrow} \end{bmatrix} \quad (2)$$

and  $\mathcal{H}_{\text{int}}(\mathbf{x})$  is the interaction (density) Hamiltonian

$$\mathcal{H}_{\text{int}} = U_0 \psi_{\uparrow}^{\dagger}(\mathbf{x}) \psi_{\downarrow}^{\dagger}(\mathbf{x}) \psi_{\downarrow}(\mathbf{x}) \psi_{\uparrow}(\mathbf{x}) \quad (3)$$

that describes the contact interaction between two atoms in different spin states with an interaction strength  $U_0$ . In the above Hamiltonian,  $\psi_{\sigma}^{\dagger}(\mathbf{x})$  and  $\psi_{\sigma}(\mathbf{x})$  are the creation and annihilation field operators of atoms in the spin-state  $\sigma = \uparrow, \downarrow$ , respectively, and  $\hat{\xi}_{\mathbf{k}} \equiv -\hbar^2 \nabla^2/(2m) - \mu$  is the single-particle kinetic energy with atomic mass  $m$ , measured with respect to the chemical potential  $\mu$ . The use of the contact interatomic interaction necessarily leads to an ultraviolet divergence at large momentum or high energy. To regularize it, the interaction strength  $U_0$  can be expressed in terms of an  $s$ -wave scattering length  $a_s$ ,

$$\frac{1}{U_0} = \frac{m}{4\pi\hbar^2 a_s} - \frac{1}{V} \sum_{\mathbf{k}} \frac{m}{\hbar^2 \mathbf{k}^2}, \quad (4)$$

where  $V$  is the volume of the system. Experimentally, the scattering length  $a_s$  can be tuned precisely to arbitrary value, by sweeping an external magnetic field across a Feshbach resonance [2], from the weakly interacting limit of Bardeen-Cooper-Schrieffer (BCS) superfluids to the strong-coupling limit of Bose-Einstein condensates (BEC) [57].

### A. Mean-field BdG theory

It is now widely known that spin-orbit coupling together with in-plane Zeeman field can induce the Fulde-Ferrell pairing, with an order parameter having a finite center-of-mass momentum along the direction of in-plane Zeeman field [27–32]. This finite-momentum pairing - also referred to as the helical phase - was first proposed in the study of noncentrosymmetric superconductors [7, 58–62]. As we apply the in-plane Zeeman field along the  $z$ -direction, we assume an order parameter

$$\Delta(\mathbf{x}) = -U_0 \langle \psi_\downarrow(\mathbf{x}) \psi_\uparrow(\mathbf{x}) \rangle = \Delta \exp(iqz) \quad (5)$$

with a FF momentum  $\mathbf{q} = q\mathbf{e}_z$ , where  $\mathbf{e}_z$  is the unit vector along the  $z$ -direction. Within the mean-field theory, we may approximate the interaction Hamiltonian as

$$\mathcal{H}_{\text{int}} \simeq - \left[ \Delta(\mathbf{x}) \psi_\uparrow^\dagger(\mathbf{x}) \psi_\downarrow^\dagger(\mathbf{x}) + \text{H.c.} \right] - \frac{\Delta^2}{U_0}. \quad (6)$$

For a Fermi superfluid, it is useful to introduce the following Nambu spinor to collectively denote the field operators,

$$\Phi(\mathbf{x}) \equiv \left[ \psi_\uparrow(\mathbf{x}), \psi_\downarrow(\mathbf{x}), \psi_\uparrow^\dagger(\mathbf{x}), \psi_\downarrow^\dagger(\mathbf{x}) \right]^T, \quad (7)$$

where the first two and last two field operators in  $\Phi(\mathbf{x})$  could be interpreted as the annihilation operators for particles and holes, respectively. The total mean-field Hamiltonian can then be written in a compact form,

$$H_{\text{mf}} = \sum_{\mathbf{k}} \hat{\xi}_{\mathbf{k}} - V \frac{\Delta^2}{U_0} + \frac{1}{2} \int d\mathbf{x} \Phi^\dagger(\mathbf{x}) \mathcal{H}_{\text{BdG}} \Phi(\mathbf{x}), \quad (8)$$

where the factor of  $1/2$  in the last term arises from the redundant use of particle and hole operators in the Nambu spinor  $\Phi(\mathbf{x})$ . Accordingly, a zero-point energy  $\sum_{\mathbf{k}} \hat{\xi}_{\mathbf{k}}$  appears in the first term, whose divergence will be removed by regularizing the bare interaction strength  $U_0$  (see below). The Bogoliubov Hamiltonian  $\mathcal{H}_{\text{BdG}}$  takes the form,

$$\mathcal{H}_{\text{BdG}} \equiv \begin{bmatrix} \hat{\xi}_{\mathbf{k}} + \lambda_z \hat{k}_z + h_{\text{in}} & \lambda_x \hat{k}_x - ih_{\text{out}} & 0 & -\Delta(\mathbf{x}) \\ \lambda_x \hat{k}_x + ih_{\text{out}} & \hat{\xi}_{\mathbf{k}} - \lambda_z \hat{k}_z - h_{\text{in}} & \Delta(\mathbf{x}) & 0 \\ 0 & \Delta^*(\mathbf{x}) & -\hat{\xi}_{\mathbf{k}} + \lambda_z \hat{k}_z - h_{\text{in}} & \lambda_x \hat{k}_x - ih_{\text{out}} \\ -\Delta^*(\mathbf{x}) & 0 & \lambda_x \hat{k}_x + ih_{\text{out}} & -\hat{\xi}_{\mathbf{k}} - \lambda_z \hat{k}_z + h_{\text{in}} \end{bmatrix}. \quad (9)$$

Note that, the spin-orbit coupling term in the hole sector of Eq. (9) does not change sign as spin-orbit coupling respects the time-reversal symmetry. The mean-field Hamiltonian Eq. (8) can be solved by taking the standard Bogoliubov transformation. In our case, it is more convenient to directly diagonalizing the Bogoliubov Hamiltonian

$$\mathcal{H}_{\text{BdG}} \Phi_{\mathbf{k}\eta}(\mathbf{x}) = E_\eta(\mathbf{k}) \Phi_{\mathbf{k}\eta}(\mathbf{x}) \quad (10)$$

with the plane-wave quasiparticle wave-function

$$\Phi_{\mathbf{k}\eta}(\mathbf{x}) \equiv \frac{e^{i\mathbf{k}\cdot\mathbf{x}}}{\sqrt{V}} \begin{bmatrix} u_{\mathbf{k}\eta\uparrow} e^{+iqz/2} \\ u_{\mathbf{k}\eta\downarrow} e^{+iqz/2} \\ v_{\mathbf{k}\eta\uparrow} e^{-iqz/2} \\ v_{\mathbf{k}\eta\downarrow} e^{-iqz/2} \end{bmatrix} \quad (11)$$

and quasiparticle energy  $E_\eta(\mathbf{k})$ . As the Bogoliubov Hamiltonian now becomes a 4 by 4 matrix, the four eigenvalues and eigenstates can be collectively specified

as  $\eta = \{\alpha, \nu\}$ , where the index  $\alpha \in (1, 2)$  indicates the upper (1) or lower (2) band split by the spin-orbit coupling and Zeeman fields, and  $\nu \in (+, -)$  stands for the particle (+) or hole (-) branch. The ansatz of the wave-function Eq. (11) is inspired by the use of the Fulde-Ferrell order parameter  $\Delta \exp(iqz)$  in the Bogoliubov Hamiltonian and is also consistent with the fact that the hole wave-function is a time-reversal partner of the particle wave-function. By substituting Eq. (11) into the Bogoliubov equation (10), we obtain a  $4 \times 4$  Bogoliubov matrix for  $[u_{\mathbf{k}\eta\uparrow}, u_{\mathbf{k}\eta\downarrow}, v_{\mathbf{k}\eta\uparrow}, v_{\mathbf{k}\eta\downarrow}]^T$ , in which the operators  $\hat{\xi}_{\mathbf{k}}$  is replaced with a  $c$ -number

$$\xi_{\mathbf{k}+\mathbf{q}/2} = \frac{\hbar^2}{2m} \left[ k_x^2 + k_y^2 + \left( k_z + \frac{q}{2} \right)^2 \right] - \mu \quad (12)$$

and  $\hat{k}_z$  replaced with  $k_z + q/2$  for the particle sector and, similarly

$$\hat{\xi}_{\mathbf{k}} \rightarrow \xi_{\mathbf{k}-\mathbf{q}/2} = \frac{\hbar^2}{2m} \left[ k_x^2 + k_y^2 + \left( k_z - \frac{q}{2} \right)^2 \right] - \mu \quad (13)$$

and  $\hat{k}_z \rightarrow k_z - q/2$  for the hole sector (see, for example, Eq. (16) below with  $-i\partial_x \rightarrow k_x$ ). Once the quasiparticle energy  $E_\eta(\mathbf{k})$  is known by diagonalizing the (complex) Bogoliubov matrix, we obtain the mean-field thermodynamic potential  $\Omega_{\text{mf}}$  at a finite temperature  $T$ :

$$\frac{\Omega_{\text{mf}}}{V} = \frac{1}{2V} \left[ \sum_{\mathbf{k}} (\xi_{\mathbf{k}+\mathbf{q}/2} + \xi_{\mathbf{k}-\mathbf{q}/2}) - \sum_{\mathbf{k}\eta} E_\eta(\mathbf{k}) \right] - \frac{\Delta^2}{U_0} - \frac{k_B T}{V} \sum_{\mathbf{k}\eta} \ln \left[ 1 + e^{-E_\eta(\mathbf{k})/k_B T} \right], \quad (14)$$

where the zero-point energy  $(1/2) \sum_{\mathbf{k}\eta} E_\eta(\mathbf{k})$  in the square bracket is again due to the redundant use of particle and hole operators, and we have rewritten the zero-point energy  $\sum_{\mathbf{k}} \hat{\xi}_{\mathbf{k}}$  to the form of  $\sum_{\mathbf{k}} (\xi_{\mathbf{k}+\mathbf{q}/2} + \xi_{\mathbf{k}-\mathbf{q}/2})/2$ , in order to cancel the leading divergence in  $(1/2) \sum_{\mathbf{k}\eta} E_\eta(\mathbf{k})$ . The last term in the thermodynamic potential accounts for the thermal excitations of Bogoliubov quasiparticles, which are non-interacting within the mean-field approximation. It worth noting that, the summation over the quasiparticle energy in  $\sum_{\mathbf{k}\eta}$  must be

restricted to  $E_\eta(\mathbf{k}) \geq 0$ , because of the inherent particle-hole symmetry of the Bogoliubov Hamiltonian.

## B. Chiral surface states and Majorana fermions

In the topological phase, the superfluid can support gapless surface states. To demonstrate this non-trivial consequence of topological order, we consider adding a hard-wall confinement in the  $x$ -direction and calculate the resulting energy spectrum  $E_n(k_z, k_y)$ . The zero-energy Majorana fermion modes are expected to appear at  $k_z = 0$  and at the two boundaries  $x = 0$  and  $x = L$  [4, 5, 54], where  $L \gg k_F^{-1}$  is the length of the confinement along the  $x$ -direction.

The use of a hard-wall potential means that the wavefunction of quasiparticles along the  $x$ -axis is no longer a plane wave. By assuming that the order parameter is approximately not affected by the confinement for sufficiently large  $L$ , we take the ansatz,

$$\Phi_{k_y k_z}(\mathbf{x}) \equiv \frac{e^{i(k_y y + k_z z)}}{\sqrt{V}} \begin{bmatrix} u_{k_y k_z \uparrow}(x) e^{+iqz/2} \\ u_{k_y k_z \downarrow}(x) e^{+iqz/2} \\ v_{k_y k_z \uparrow}(x) e^{-iqz/2} \\ v_{k_y k_z \downarrow}(x) e^{-iqz/2} \end{bmatrix}. \quad (15)$$

By substituting Eq. (15) into Eq. (9), the resulting BdG Hamiltonian for a given set of  $(k_z, k_y)$  has the form,

$$\mathcal{H}_{\text{BdG}} = \begin{bmatrix} -\frac{\hbar^2}{2m} \partial_x^2 + \tilde{H}_{11}^{(p)} & i(-\lambda_x \partial_x - h_{\text{out}}) & 0 & -\Delta \\ i(-\lambda_x \partial_x + h_{\text{out}}) & -\frac{\hbar^2}{2m} \partial_x^2 + \tilde{H}_{22}^{(p)} & \Delta & 0 \\ 0 & \Delta & +\frac{\hbar^2}{2m} \partial_x^2 + \tilde{H}_{11}^{(h)} & i(-\lambda_x \partial_x - h_{\text{out}}) \\ -\Delta & 0 & i(-\lambda_x \partial_x + h_{\text{out}}) & +\frac{\hbar^2}{2m} \partial_x^2 + \tilde{H}_{22}^{(h)} \end{bmatrix}, \quad (16)$$

where

$$\tilde{H}_{11}^{(p)} = + \left[ \frac{\hbar^2}{2m} \left( k_y^2 + k_z^2 + \frac{q^2}{4} \right) - \mu \right] + \frac{\hbar^2}{2m} q k_z + \lambda_z \left( k_z + \frac{q}{2} \right) + h_{\text{in}}, \quad (17)$$

$$\tilde{H}_{22}^{(p)} = + \left[ \frac{\hbar^2}{2m} \left( k_y^2 + k_z^2 + \frac{q^2}{4} \right) - \mu \right] + \frac{\hbar^2}{2m} q k_z - \lambda_z \left( k_z + \frac{q}{2} \right) - h_{\text{in}}, \quad (18)$$

$$\tilde{H}_{11}^{(h)} = - \left[ \frac{\hbar^2}{2m} \left( k_y^2 + k_z^2 + \frac{q^2}{4} \right) - \mu \right] + \frac{\hbar^2}{2m} q k_z + \lambda_z \left( k_z - \frac{q}{2} \right) - h_{\text{in}}, \quad (19)$$

$$\tilde{H}_{22}^{(h)} = - \left[ \frac{\hbar^2}{2m} \left( k_y^2 + k_z^2 + \frac{q^2}{4} \right) - \mu \right] + \frac{\hbar^2}{2m} q k_z - \lambda_z \left( k_z - \frac{q}{2} \right) + h_{\text{in}}. \quad (20)$$

To diagonalize the BdG Hamiltonian Eq. (16), we expand all the quasiparticle wavefunctions in terms of the single-particle eigenstates of the hard-wall potential,

which is given by

$$\psi_l(x) = \sqrt{\frac{2}{L}} \sin \left( \frac{l\pi x}{L} \right), \quad (21)$$

with an integer  $l = 1, 2, 3, \dots$ . For example, for  $u_{k_y k_z \uparrow}(x)$

we have

$$u_{k_y k_z \uparrow}(x) = \sum_{l=1}^{N_{\max}} u_{k_y k_z \uparrow}^{(l)} \psi_l(x), \quad (22)$$

where  $N_{\max} \gg 1$  is a high energy cut-off. This converts the BdG Hamiltonian Eq. (16) into a  $4N_{\max}$  by  $4N_{\max}$  symmetric matrix, with the matrix elements,

$$[-\partial_x^2]_{lm} = \left(\frac{\pi l}{L}\right)^2 \delta_{lm} \quad (23)$$

and

$$[\partial_x]_{lm} = \frac{m}{L} \left[ \frac{1 - \cos \pi(l+m)}{(l+m)} + \frac{1 - \cos \pi(l-m)}{(l-m)} \right]. \quad (24)$$

The diagonalization leads directly to the energies  $E_n(k_y, k_z)$  and wavefunctions of the chiral surface states.

### III. RESULTS AND DISCUSSIONS

For a uniform Fermi gas, we use the natural units,  $2m = \hbar = k_B = k_F = E_F = 1$ . This means that we take the Fermi wavevector  $k_F$  and Fermi energy  $E_F$  as the units for wavevector and energy. Thus, the spin-orbit coupling will be parameterized by the dimensionless parameter  $\tilde{\lambda}_{z,x} = \lambda_{z,x} k_F / E_F$ . It is also understood that for the Zeeman fields we use  $\tilde{h}_{\text{in}} = h_{\text{in}} / E_F$  and  $\tilde{h}_{\text{out}} = h_{\text{out}} / E_F$ . To find possible mean-field phases, for a given set of parameters (including spin-orbit coupling  $\lambda k_F / E_F$ , Zeeman field  $h / E_F$ , interaction parameter  $1 / (k_F a_s)$ , and temperature  $T / T_F$ ) and total density  $N / V = k_F^3 / (3\pi^2) = 1 / (3\pi^2)$ , we need to minimize the mean-field thermodynamic potential against  $\Delta$  and  $q$ , i.e.,

$$\frac{\partial \Omega_{\text{mf}}}{\partial \Delta} = 0, \quad (25)$$

$$\frac{\partial \Omega_{\text{mf}}}{\partial q} = 0. \quad (26)$$

Moreover, we have the number equation,

$$-\frac{1}{V} \frac{\partial \Omega_{\text{mf}}}{\partial \mu} = \frac{N}{V} = \frac{1}{3\pi^2}. \quad (27)$$

These equations are solved self-consistently by using Newton's gradient approach. The various derivatives can be approximated by numerical differences. The approach is very efficient, provided a good guess of the initial parameters, which may be obtained by plotting the contour plot of the mean-field thermodynamic potential. Throughout the paper, we focus on the BCS side with a dimensionless interaction parameter  $1 / (k_F a_s) = -0.5$  and use mean-field theory to solve the model Hamiltonian at both zero and finite temperatures. The spin-orbit coupling strength is always fixed to  $\lambda = E_F / k_F$ . In most cases, we consider a Rashba spin-orbit coupling. The deviation from the Rashba case will be investigated at the end of the section.

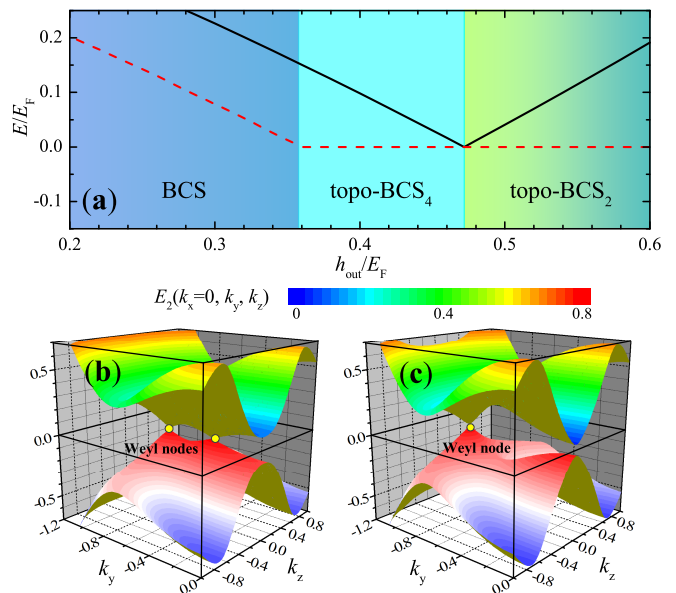


FIG. 2: (Color online). (a) Evolution of the superfluid phase with increasing the out-of-plane Zeeman field, at zero in-plane Zeeman field  $h_{\text{in}} = 0$ . The system evolves from a standard BCS superfluid to a topological non-trivially superfluid with either four (topo-BCS<sub>4</sub>) or two Weyl nodes (topo-BCS<sub>2</sub>). The solid and dashed lines show the energy at  $\mathbf{k} = 0$  [ $E_{2+}(\mathbf{k} = 0)$ ] and the minimum energy [ $\min E_{2+}(\mathbf{k})$ ] of the lower particle branch. (b) and (c) show the characteristic quasiparticle excitation spectrum  $E_{2\pm}(k_x = 0, k_y, k_z)$  in the topo-BCS<sub>4</sub> ( $h_{\text{out}} = 0.4E_F$ ) and topo-BCS<sub>2</sub> phases ( $h_{\text{out}} = 0.5E_F$ ), respectively. We note that the spectrum is symmetric with respect to  $k_y$  and we plot only the left part with  $k_y \leq 0$ .

#### A. Zero temperature phase diagram

##### 1. Out-of-plane Zeeman field

Let us first consider the simplest case with an out-of-plane Zeeman field only, a situation that was previously addressed by Gong and co-workers [15]. The zero-temperature phase diagram is reported in Fig. 2(a), together with the energy spectra of two topologically non-trivial phases at  $h_{\text{out}} = 0.4E_F$  and  $h_{\text{out}} = 0.5E_F$  in Figs. 2(b) and 2(c), respectively. The chiral surface states in the presence of a hard-wall confinement at the two boundaries along the  $x$ -direction are shown in Fig. 3.

In the phase diagram, the properties of any possible 3D phase can be understood by *dimensional reduction* in momentum space to a set of 2D phases [4, 55]. The basic idea of dimensional reduction is to treat the 3D Hamiltonian, for example,  $\mathcal{H}_{\text{BdG}}(\hat{k}_x, \hat{k}_y, \hat{k}_z)$  of the 3D bulk system, Eq. (9) or Eq. (16) - which is translationally invariant along the  $y$ -direction (and therefore the momentum operator  $\hat{k}_y$  can simply be replaced with a  $c$ -number  $k_y$ ) - as a set of 2D systems, i.e.,

$$\mathcal{H}_{\text{BdG}}(\hat{k}_x, \hat{k}_y, \hat{k}_z) = \sum_{k_y} \mathcal{H}_{k_y}^{(2D)}(\hat{k}_x, \hat{k}_z), \quad (28)$$



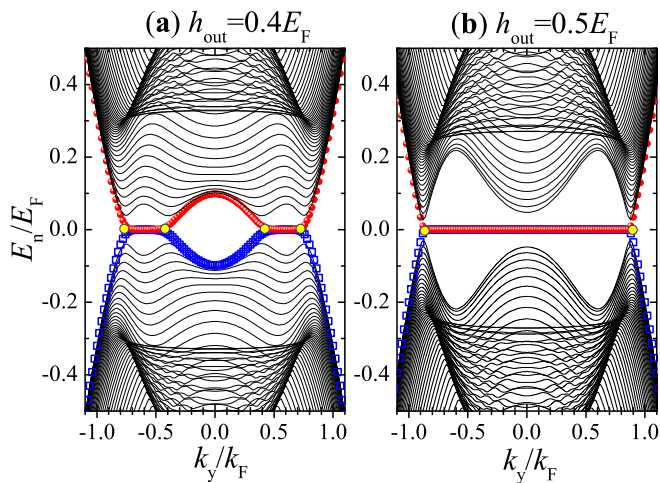


FIG. 3: (Color online). Chiral surface modes - highlighted by blue empty squares and red solid circles - with a hard-wall confinement along the  $x$ -direction at  $k_z = 0$ , in the topo-BCS<sub>4</sub> (a) or topo-BCS<sub>2</sub> phases (b). The system may be viewed as a stack of many 2D topological superfluids along the  $y$ -direction. Accordingly, the surface modes of the system may be understood as a collection of the edge modes of these 2D systems.

each of which is described by an effective 2D Hamiltonian  $\mathcal{H}_{k_y}^{(2D)}(\hat{k}_x, \hat{k}_z)$  parameterized by  $k_y$ . In the context of topological insulators and superfluids [4], this idea was successfully used to understand the classification of 3D topological states. A *weak* 3D topological phase can be defined, as a stack of 2D topological phases, which are *dispersionless* along the  $y$ -direction. Actually, this is exactly the case happened in our 3D system. We claim the existence of a 3D topological phase if there is an effective 2D Hamiltonian with suitable  $k_y$  that can host a topological phase. The chiral surface states of the 3D topological phase may simply be understood as the edge states of many 2D systems accumulated along the  $y$ -axis and characterized by a good quantum number  $k_y$  (see Fig. 3). The dispersion of these surface states in other directions can be obtained from the dispersion of the edge states [55]. It is worth noting that this scenario of dimensional reduction works for arbitrary in-plane and out-of-plane Zeeman fields. Numerically, it is convenient to identify a 3D topological phase by looking at whether there are chiral surface states or not.

In the presence of an out-of-plane Zeeman field  $h_{\text{out}}$  only, it is known that the 2D Hamiltonian  $\mathcal{H}_{k_y}^{(2D)}(\hat{k}_x, \hat{k}_z)$  supports a topological phase when the field strength  $h_{\text{out}}$  is above a threshold [4, 12, 17]. The topological phase transition is accompanied by the closing and re-opening of the bulk quasiparticle excitation gap at  $k_x = 0$  and  $k_z = 0$ , which from Eq. (9) is given by [15],

$$E_g = 2 \left| h_{\text{out}} - \sqrt{[\mu(k_y)]^2 + \Delta^2} \right|, \quad (29)$$

where  $\mu(k_y) \equiv \mu - \hbar^2 k_y^2 / (2m)$  is a “local” chemical po-

tential for the slice with  $k_y$  in momentum space, and the chemical potential  $\mu$  and pairing gap  $\Delta$  themselves are functions of the out-of-plane Zeeman field  $h_{\text{out}}$ . Thus, the transition occurs at the threshold

$$h_{\text{out}}^{(c)} = \sqrt{[\mu(k_y)]^2 + \Delta^2}, \quad (30)$$

whose value depends critically on  $k_y$ . Due to a positive chemical potential  $\mu$  on the BCS side, it is easy to see that the topological phase transition first occurs at  $\pm k_y^{(c)} \neq 0$ .

By increasing the out-of-plane Zeeman field, the slices with  $k_y \in [-k_2^{(W)}, -k_1^{(W)}] \cup [k_1^{(W)}, k_2^{(W)}]$  become topologically non-trivial (see, for example, Fig. 3(a)). The momenta  $\pm k_1^{(W)}$  and  $\pm k_2^{(W)}$ , satisfying  $k_1^{(W)} < k_y^{(c)} < k_2^{(W)}$ , are four boundary points at which the excitation gap must close. These are the so-called Weyl nodes, around each of which the effective Hamiltonian describes quasiparticles with a linear dispersion that resembles a 3D Dirac cone (see Fig. 2(b) for the two Weyl nodes at  $k_y < 0$ ). These Dirac cone spectra are very robust against any perturbation of the bulk Hamiltonian  $\mathcal{H}_{BdG}$  and are topologically protected by a topological invariant [15, 55]. They are exactly an ultracold-atom analog of Weyl fermions of particle physics. In this respect, we may refer to the topological phase as a Weyl superfluid. Due to the existence of Weyl nodes, we see immediately that the global energy gap in the topological phase must vanish. By further increasing the out-of-plane Zeeman field, the lower bound momentum  $k_1^{(W)}$  may become zero and therefore the two inner Weyl nodes (with *opposite* topological invariant) annihilate with each other. This happens when the local energy gap at  $\mathbf{k} = 0$  closes. Afterwards, the system supports two Weyl nodes.

From the above analysis, it is clear that the appearance of a topological phase with four and two Weyl nodes can be determined by the closing of the global energy gap and of the local energy gap at  $\mathbf{k} = 0$ , respectively. This is demonstrated in Fig. 2(a), where we plot the minimum energy [ $\min E_{2+}(\mathbf{k})$ ] and the local energy at  $\mathbf{k} = 0$  [ $E_{2+}(\mathbf{k} = 0)$ ] of the lower particle branch by using the dashed and solid lines, respectively. Here we use the minimum energy, instead of a global energy gap  $E_g = 2 |\min E_{2+}(\mathbf{k})|$  that is the energy difference between the minimum energy of the particle branch and the maximum of the hole branch due to the particle-hole symmetry  $E_{2+}(\mathbf{k}) = -E_{2-}(-\mathbf{k})$ . As we shall see below, the minimum energy is more useful to characterize the emergence of gapless phase [43]. With increasing out-of-plane Zeeman field, the minimum energy develops a zero-energy *plateau* as the system enters the topological phase, due to the occasional band touching of the particle and hole branches at Weyl nodes. In contrast, the local energy at  $\mathbf{k} = 0$  will close and then reopen at the critical field where the number of Weyl nodes decreases from four to two.

In the topological phase, the formation of isolated Weyl nodes can be clearly identified in the energy spectrum in momentum space, as shown in Figs. 2(b) and 2(c). It

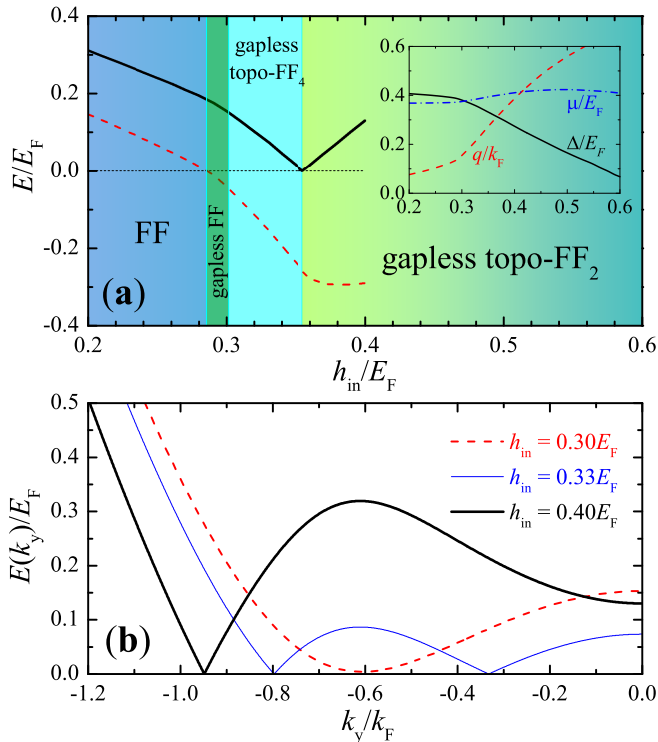


FIG. 4: (Color online). (a) Evolution of the superfluid phase with increasing the in-plane Zeeman field, at zero out-of-plane Zeeman field  $h_{\text{out}} = 0$ . Driven by the in-plane field only, the system evolves from a gapped FF superfluid to a gapless FF state, and then to a topologically non-trivial FF superfluid with either four (gapless topo-FF<sub>4</sub>) or two Weyl nodes/loops (gapless topo-FF<sub>2</sub>). The solid and dashed lines show the energy at  $\mathbf{k} = 0$  [ $E_{2+}(\mathbf{k} = 0)$ ] and the minimum energy [ $\min E_{2+}(\mathbf{k})$ ] of the lower particle branch. The inset shows the chemical potential, pairing gap and FF pairing momentum as a function of the in-plane Zeeman field. (b) The energy of the lower particle branch along the  $k_y$ -direction,  $E_{2+}(k_x = 0, k_y, k_z = 0)$ , at  $h_{\text{in}}/E_F = 0.30$  (gapless FF, dashed line), 0.33 (gapless topo-FF<sub>4</sub>, thin solid line) and 0.40 (gapless topo-FF<sub>2</sub>, thick solid line). The minimum energy touches zero at the positions of Weyl nodes.

is interesting that these Weyl nodes are connected continuously by zero-energy Majorana surface states once we impose the hard-wall confinement at the two boundaries along the  $x$ -direction (see Fig. 3). The existence of the Majorana modes is easy to understand from the dimensional reduction mentioned earlier: the surface states with a given  $k_y$  and  $k_z$  of the 3D Hamiltonian  $\mathcal{H}_{BdG}$  is a sum of the edge state with momentum  $k_z$  of the 2D Hamiltonian in Eq. (28) with  $k_y$  as a parameter value. For  $k_z = 0$ , all the edge states have zero-energy at any value of  $k_y$  in the range where the 2D slice is topologically nontrivial and, therefore, they form a Majorana flat band [55, 63].

To close this subsection, we note that, with a small in-plane Zeeman field, the phase diagram is essentially unchanged. The only difference is that Cooper pairs now

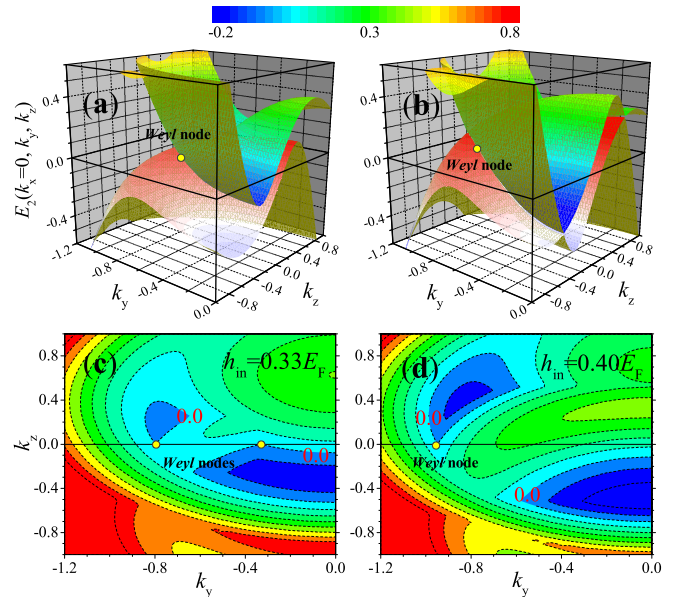


FIG. 5: (Color online). The characteristic quasiparticle excitation spectrum  $E_{2\pm}(k_x = 0, k_y, k_z)$  in the gapless topo-FF<sub>4</sub> phase with  $h_{\text{in}} = 0.33E_F$  (a) and in the gapless topo-FF<sub>2</sub> phase with  $h_{\text{in}} = 0.40E_F$  (b). The corresponding contour plots of  $E_{2+}(k_x = 0, k_y, k_z)$  are shown in (c) and (d), respectively. The Weyl nodes are highlighted by yellow solid circles. We note that the out-of-plane Zeeman field  $h_{\text{out}} = 0$ . The spectrum is symmetric with respect to  $k_y$ , so we plot only the left part with  $k_y \leq 0$ .

acquire a finite center-of-mass momentum. The resulting topologically nontrivial phases are better referred to as topo-FF<sub>4</sub> or topo-FF<sub>2</sub>, according to the number of Weyl nodes. The linear quasiparticle spectrum around a Weyl node becomes anisotropic [44]. In the presence of a large in-plane Zeeman field, however, the phase diagram would change qualitatively, as we now turn to discuss in great detail.

## 2. In-plane Zeeman field

Figure 4(a) reports the phase diagram in the presence of an in-plane Zeeman field only. Compared with Fig. 2, with increasing the Zeeman field strength, the local energy at  $\mathbf{k} = 0$  (solid line) shows similar behavior. On the contrary, the minimum energy  $\min E_{2+}(\mathbf{k})$  (dashed line) exhibits very different field dependence. It becomes negative at  $h_{\text{in}} > h_{\text{in}}^{(\text{gapless})} \simeq 0.284E_F$  and indicates clearly that the spin-orbit coupled Fermi gas enters a gapless phase, due to the existence of a significant Fulde-Ferrell pairing momentum at the order of Fermi momentum (i.e.,  $q \sim k_F$ , see the inset). It is natural to ask: would the gapless system become topologically non-trivial at a larger in-plane Zeeman field  $h_{\text{in}}^{(c)} > h_{\text{in}}^{(\text{gapless})}$ ?

Our answer is yes, after a careful check on the structure of the energy spectrum (Fig. 5) as well as the appearance

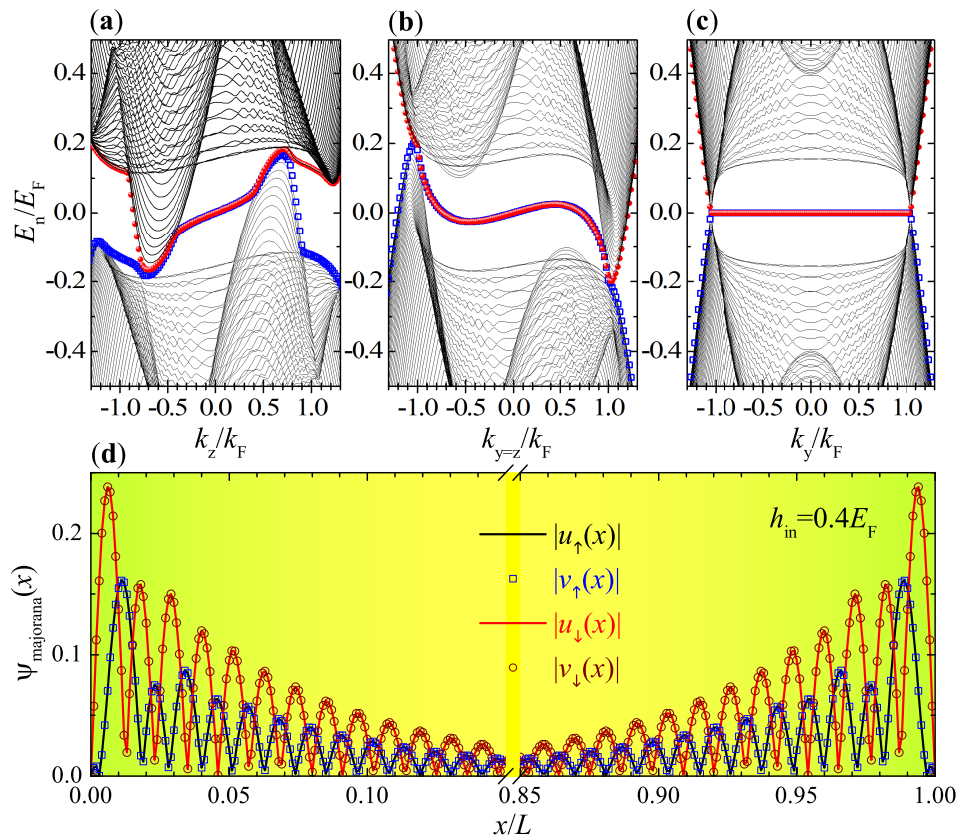


FIG. 6: (Color online). Chiral surface modes with a hard-wall confinement along the  $x$ -direction in the gapless topo-FF<sub>2</sub> phase ( $h_{\text{in}} = 0.4E_F$ ), at  $k_y = 0$  (a), along the  $k_y = k_z$  line (b), or at  $k_z = 0$  (c). The wave-functions of the Majorana mode at  $k_y = k_z = 0$  is shown in (d), which are well localized at the two boundaries  $x = 0$  and  $x = L = 200k_F^{-1}$ .

of the Majorana surface states (Fig. 6). The energy spectrum can have Weyl nodes as the in-plane Zeeman field  $h_{\text{in}} > h_{\text{in}}^{(c1)} \simeq 0.301E_F$ . This is particularly clear when we plot the spectrum at  $k_x = k_z = 0$  as a function of the parameterized momentum  $k_y$  [64], as shown in Fig. 4(b). Resembling the earlier case with an out-of-plane Zeeman field, four Weyl nodes develop once  $h_{\text{in}} > h_{\text{in}}^{(c1)}$  in the gapless topo-FF<sub>4</sub> phase. In addition, by further increasing the in-plane Zeeman field above a threshold  $h_{\text{in}}^{(c2)} \simeq 0.355E_F$ , exactly at which the local energy gap at  $\mathbf{k} = 0$  closes, the number of nodes decreases to two in the gapless topo-FF<sub>2</sub> phase. There is, however, a notable difference when we examine the full energy spectrum in Fig. 5. In the gapless phase, the nodal points will enclose and form two surfaces, one in the particle branch and another in the hole branch [31]. Along the cut  $k_x = 0$ , as shown in Figs. 5(c) and 5(d), each Weyl node will then extend to form a closed loop (i.e., Weyl loop). Nevertheless, the occasional band touching of the particle and hole branches still occurs at a single point on the  $k_z = 0$  axis and therefore the topological nature of the spectrum remains unchanged.

In Figs. 6(a), 6(b) and 6(c), we present the energy dispersion of the surface states in the gapless topo-FF<sub>2</sub> phase. At  $k_z = 0$  (Fig. 6(c)), we observe the same Majorana

flat band as in the case of out-of-plane Zeeman field (see, for example, Fig. 3(b)), which connects the two Weyl nodes in the bulk spectrum. To confirm that the surface states are indeed zero-energy Majorana modes, in Fig. 6(d) we plot the wave-function of one of the surface states at  $k_y = k_z = 0$ . The wave-function is well localized at the two boundaries and satisfies the desired symmetry  $u_{\sigma}(x) = e^{i\theta} v_{\sigma}^*(x)$  ( $\sigma = \uparrow, \downarrow$ ) for Majorana modes. It is interesting that with an in-plane Zeeman field, the topological superfluid may support *unidirectional* chiral surface states, as demonstrated in Figs. 6(a) and 6(b), which propagate in the same direction at the opposite boundaries with the same velocity  $v = \partial E / \partial k$  [43]. As discussed in Ref. [43], such unidirectional surface states are actually a smoking-gun feature of the gapless topological superfluid. Similar to the Majorana flat band, the unidirectional chiral surface states also connect some points in the bulk spectrum, at which the particle and hole branches touch with each other and the local spectrum is approximately linear.

Our results of in-plane Zeeman field induced gapless topological superfluids are not captured by a previous study based on the same model Hamiltonian [44]. In that work, in the absence of an out-of-plane Zeeman field, the system was thought to always be in the gapless Fulde-



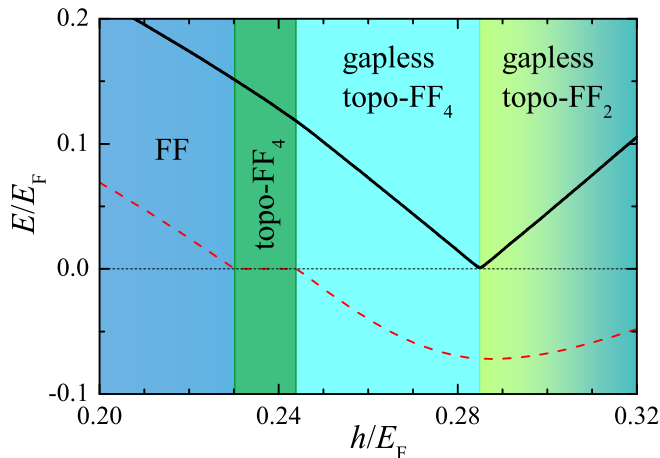


FIG. 7: (Color online). (a) Evolution of the superfluid phase with equally increasing the in-plane and out-of-plane Zeeman fields (i.e.,  $h_{\text{in}} = h_{\text{out}} = h$ ). The system evolves from a gapped FF superfluid to a gapped topologically nontrivial topo-FF<sub>4</sub> state, and then to a gapless topologically non-trivial FF superfluid with either four (gapless topo-FF<sub>4</sub>) or two Weyl nodes/loops (gapless topo-FF<sub>2</sub>). The solid and dashed lines show the energy at  $\mathbf{k} = 0$  [ $E_{2+}(\mathbf{k} = 0)$ ] and the minimum energy [ $\min E_{2+}(\mathbf{k})$ ] of the lower particle branch.

Ferrell superfluid [44]. This discrepancy may originate from a different definition of topological phase for the 2D slices, in the view of dimensional reduction. On the other hand, we are not able to produce the contour plot of the zero-energy quasiparticle spectrum at a large in-plane Zeeman field, as shown by the blue line in Fig. 2(b) of Ref. [44], which has *connected* closed lines for nodal points and therefore was thought topologically trivial. The contour plots in our Figs. 5(c) and 5(d) are rather similar to the one with a small out-of-plane Zeeman field as shown by the red line in Fig. 2(b) of Ref. [44], which was also regarded by those authors as topologically non-trivial.

### 3. Equal in-plane and out-of-plane Zeeman fields

We now consider another special case with equal in-plane and out-of-plane Zeeman fields. Figure 7 shows the phase diagram determined by monitoring the minimum energy and the local energy at  $\mathbf{k} = 0$  of the lower particle branch. The contour plots of the energy spectrum at  $k_x = 0$  in different superfluid phases are reported in color in Fig. 8. A gapped topological Fulde-Ferrell phase can be easily identified from the zero-energy plateau in the minimum energy. A close look at the energy spectrum (Fig. 8(b)) indicates that this phase has four Weyl nodes and therefore should be classified as a topo-FF<sub>4</sub> phase. With increasing the Zeeman field, nodal points develop in the energy spectrum and the system enters the gapless topological phase with four (Fig. 8(c)) and then two Weyl nodes (Fig. 8(d)).

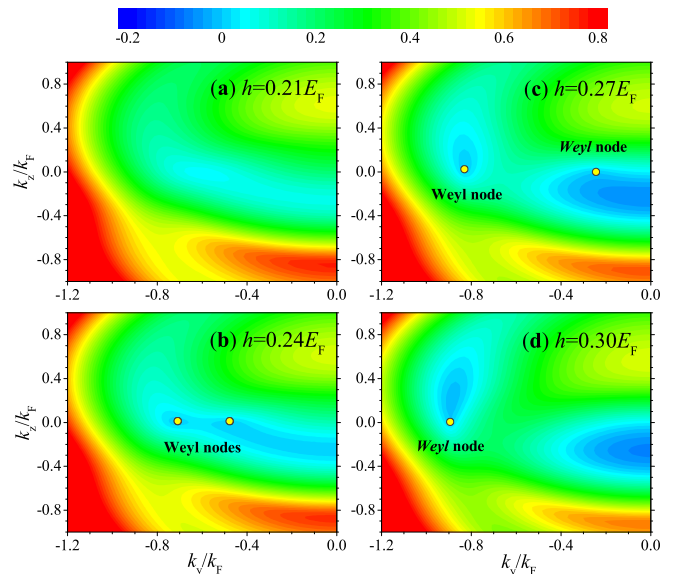


FIG. 8: (Color online). Contour plots of the particle branch  $E_{2+}(\mathbf{k})$  in the gapped FF phase (a), the gapped topo-FF<sub>4</sub> phase (b), the gapless topo-FF<sub>4</sub> phase (c), and the gapless topo-FF<sub>2</sub> phase (d). The Weyl nodes are highlighted by yellow solid circles. We note that the in-plane and out-of-plane Zeeman fields are equal,  $h_{\text{in}} = h_{\text{out}} = h$ . The spectrum is symmetric with respect to  $k_y$ , so we plot only the left part with  $k_y \leq 0$ .

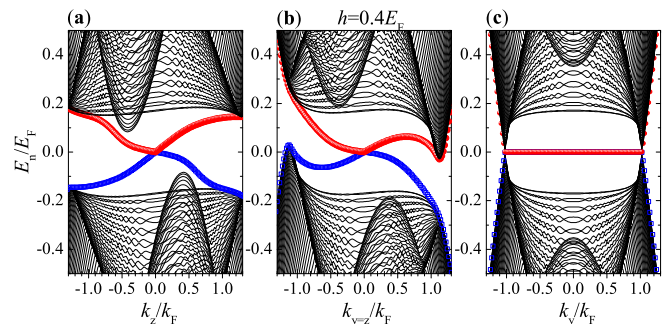


FIG. 9: (Color online). Chiral surface modes with a hard-wall confinement along the  $x$ -direction in the gapless topo-FF<sub>2</sub> phase ( $h_{\text{in}} = h_{\text{out}} = 0.4E_F$ ), at  $k_y = 0$  (a), along the  $k_y = k_z$  line (b), or at  $k_z = 0$  (c).

In Fig. 9, we show the chiral surface modes in the gapless topo-FF<sub>2</sub> phase with  $h_{\text{in}} = h_{\text{out}} = 0.4E_F$ . Along the cut  $k_z = 0$  as shown in Fig. 9(c), we again find the Majorana flat band as a function of the parameterized momentum  $k_y$ . This is indeed a very robust feature of our system as the Hamiltonian is dispersionless along the  $k_y$ -axis. When we make cuts along other directions, i.e., along the  $k_y = 0$  and  $k_y = k_z$  axis in Figs. 9(a) and 9(b), the surface states do have dispersion. They propagate along the opposite direction at the two boundaries, as a result of the *gapped* energy spectrum along the cuts [43], although the topological phase itself is globally gapless in the bulk.

#### 4. Phase diagram on the $h_{in}$ - $h_{out}$ plane

By tuning in-plane and out-of-plane Zeeman fields, we obtain the zero-temperature phase diagram, as displayed earlier in Fig. 1. The solid line, which separates a usual Fulde-Ferrell superfluid from a topologically non-trivial Fulde-Ferrell superfluid, is determined by the first appearance of Weyl nodes in the energy of the lower particle branch along the  $k_y$ -direction,  $E_{2+}(k_x = 0, k_y, k_z = 0)$  (see, for example, Fig. 4(b)). The transition within different topological phases (i.e., from four to two Weyl nodes), shown by the dot-dashed line, can be conveniently determined by the closing of the local energy gap at origin, i.e.,  $E_{2+}(\mathbf{k} = \mathbf{0}) = 0$ . On the other hand, the gapless transition indicated by red solid circles in the figure could be obtained from the critical field at which the minimum energy  $\min E_{2+}(\mathbf{k})$  becomes negative. It is worth noting that the red solid circles are not smoothly connected. Physically, on the left-hand side of these solid circles, the topological phase has occasionally touched Weyl nodes along the  $k_y$ -axis, while on their right-hand side, each Weyl node extends to form a loop of nodal points on the  $k_y$ - $k_z$  plane, as we already discussed in Figs. 5(c) and 5(d).

It is impressive that on the BCS side the topological Fulde-Ferrell phases, either gapped or gapless, dominate in the phase diagram. In particular, the gapless topological Fulde-Ferrell superfluid with two Weyl nodes is already energetically favorable at a moderately large in-plane Zeeman field (i.e.,  $h_{in} > 0.35E_F$ ).

#### B. Finite-temperature phase diagram

In current cold-atom laboratories, the lowest accessible experimental temperature is about  $0.05 - 0.1T_F$  [65]. It is thus useful to consider how the different superfluid phases involve as temperature increases. In Figs. 10, 11 and 12, we show the finite-temperature phase diagrams at different configurations of Zeeman fields. Our mean-field theory is less reliable at finite temperature. However, on the BCS side with a weak interaction parameter  $1/(k_F a_s) = -0.5$ , we anticipate that it will provide a very good semi-quantitative description.

In the presence of out-of-plane Zeeman field (Fig. 10), the finite-temperature phase diagram has been earlier discussed by Seo and co-workers [34]. It contains two topological BCS phases and is relatively easy to understand. In the other two cases with in-plane Zeeman field only (Fig. 11) or equal in-plane and out-of-plane Zeeman fields (Fig. 12), gapless topological Fulde-Ferrell superfluids emerge at sufficiently large field strength. It is remarkable that the phase space for these gapless topological superfluids is very significant at finite temperature. In particular, when the system is cooled down from a normal state at high temperature, the pairing instability first occurs towards the formation of gapless topological phases. The typical superfluid transition temperature is

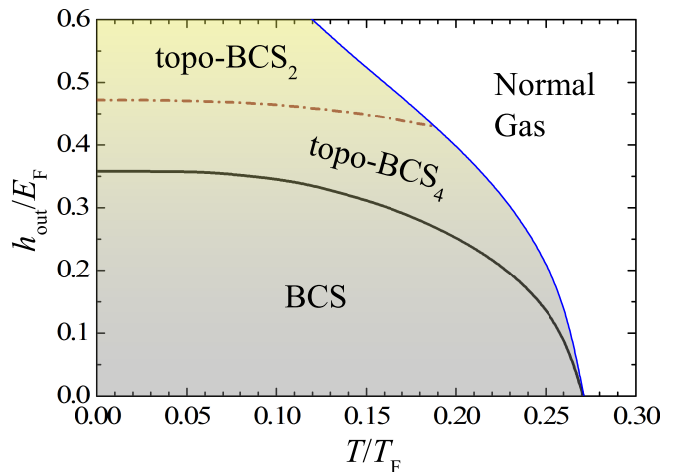


FIG. 10: (Color online). Finite temperature phase diagram on the  $T$ - $h_{out}$  plane at zero in-plane Zeeman field  $h_{in} = 0$ .

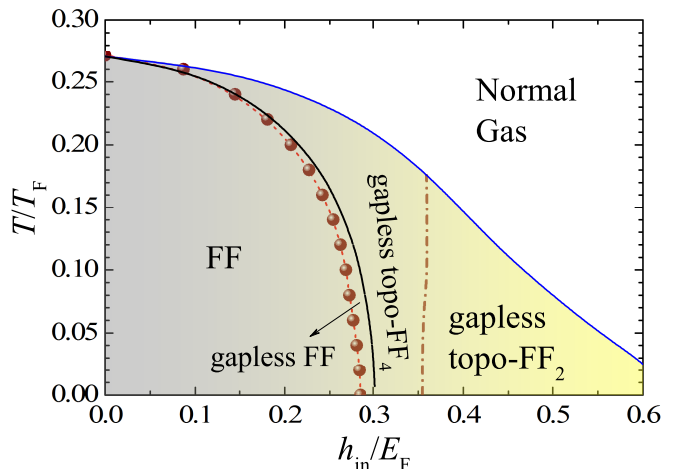


FIG. 11: (Color online). Finite temperature phase diagram on the  $h_{in}$ - $T$  plane at zero out-of-plane Zeeman field  $h_{out} = 0$ .

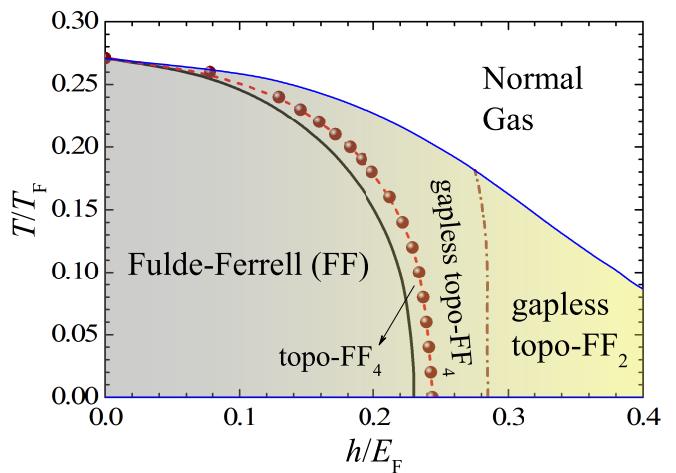


FIG. 12: (Color online). Finite temperature phase diagram on the  $h$ - $T$  plane with equal in-plane and out-of-plane Zeeman fields  $h_{in} = h_{out} = h$ .

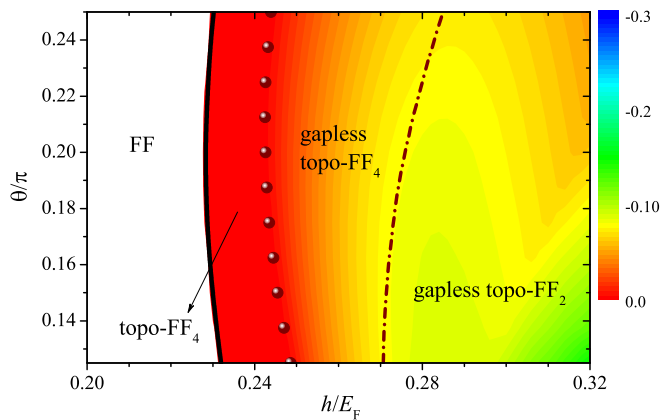


FIG. 13: (Color online). Zero-temperature phase diagram with an anisotropic spin-orbit coupling  $\lambda(\cos\theta\hat{k}_z\sigma_z + \sin\theta\hat{k}_x\sigma_x)$  and equal in-plane and out-of-plane Zeeman fields  $h_{\text{in}} = h_{\text{out}} = h$ . The Rashba spin-orbit coupling corresponds to the case with  $\theta = \pi/4$ . The color map shows the lowest energy in the particle branches, in units of  $E_F$ . Here, we use a spin-orbit coupling strength  $\lambda = E_F/k_F$  and an interaction strength  $1/(k_F a_s) = -0.5$ .

about  $0.15T_F$ , which is clearly within the reach in current cold-atom experiments [65].

### C. Phase diagram with imperfect Rashba spin-orbit coupling

We now turn to consider a general form of spin-orbit coupling with  $\lambda_z = \lambda \cos\theta$  and  $\lambda_x = \lambda \sin\theta$ , away from the Rashba spin-orbit coupling that corresponds to  $\theta = \pi/4$ . This investigation is helpful for future experiments, as the synthetic spin-orbit coupling - to be realized in cold-atom laboratories - may not acquire the perfect form of Rashba spin-orbit coupling. In Fig. 13, we show the evolution of the zero-temperature phase diagram as a function of the angle  $\theta$  down to  $\theta = \pi/8$ , in the presence of equal in-plane and out-of-plane Zeeman fields. The Zeeman field dependence of the minimum energy  $\min E_{2+}(\mathbf{k})$  and the local energy at  $\mathbf{k} = 0$   $E_{2+}(\mathbf{k} = 0)$  of the lower particle branch in the case of  $\theta = \pi/8$ , where the component of Dresselhaus spin-orbit coupling becomes significant, are reported in Fig. 14(a).

The phase diagram is less affected by tuning the form of spin-orbit coupling. With decreasing  $\theta$ , the phase space for the topological phases (including gapped or gapless topo-FF<sub>4</sub>, and gapless topo-FF<sub>2</sub>) is essentially unchanged. It is remarkable that the most interesting gapless topo-FF<sub>2</sub> phase seems to be more favorable away from the Rashba spin-orbit coupling. This could be attributed to the increasing Fulde-Ferrell momentum  $q$  at large Zeeman field, as shown in Fig. 14(b), which favors the gapless phase and also the topological phase with two Weyl nodes.

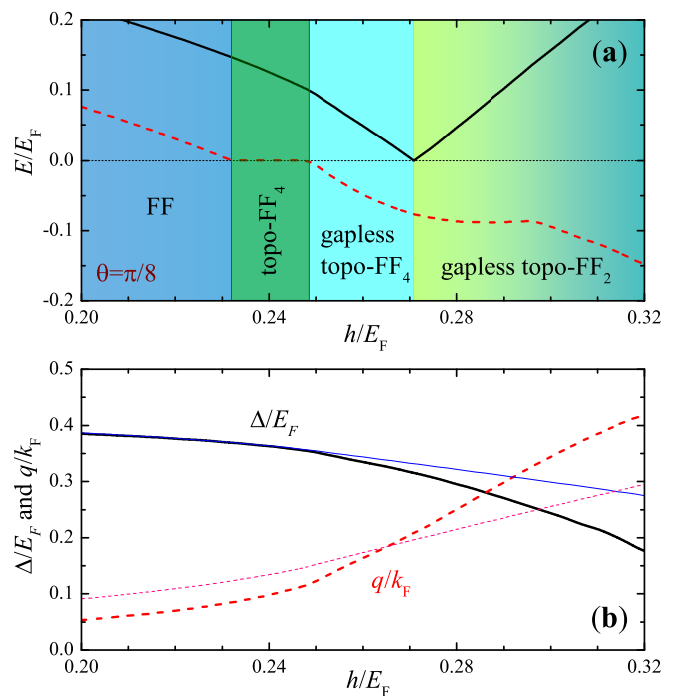


FIG. 14: (Color online). (a) Evolution of the superfluid phase with equally increasing the in-plane and out-plane Zeeman fields, and with an imperfect Rashba spin-orbit coupling at the angle  $\theta = \pi/8$ . The system evolves from a gapped FF superfluid to a gapped topologically nontrivial topo-FF<sub>4</sub> state, and then to a gapless topologically non-trivial FF superfluid with either four (gapless topo-FF<sub>4</sub>) or two Weyl nodes/loops (gapless topo-FF<sub>2</sub>). The solid and dashed lines show the energy at  $\mathbf{k} = 0$  [ $E_{2+}(\mathbf{k} = 0)$ ] and the minimum energy [ $\min E_{2+}(\mathbf{k})$ ] of the lower particle branch. (b) The pairing gap (solid line) and FF pairing momentum (dashed line) as a function of the Zeeman field. The thick and thin lines correspond to the cases with  $\theta = \pi/8$  and  $\theta = \pi/4$ , respectively.

## IV. CONCLUSIONS

In conclusions, we have presented a systematic investigation of the superfluid phases of a spin-orbit coupled Fermi gas with both in-plane and out-of-plane Zeeman fields, by using a dimensional reduction picture [55]. Driven by large Zeeman fields, in particular, the large in-plane Zeeman field, the system supports a number of intriguing features including Fulde-Ferrell pairing, topological superfluids with Majorana fermions in real space and Weyl fermions in momentum space, and also novel gapless topological superfluids. We have considered the phase diagram at both zero temperature and finite temperature. We have mainly focused on Rashba spin-orbit coupling. The case with an imperfect Rashba spin-orbit coupling has also been addressed, from a realistic experimental point of view. Our work complements the earlier investigation by Xu and co-workers [44], by providing a richer phase diagram at zero temperature and extended phase diagrams at finite temperature and with more gen-

eral spin-orbit coupling.

In future studies, it will be useful to consider the pair fluctuations which become very significant at the BEC-BCS crossover at both zero and finite temperatures. The finite-temperature pair fluctuations for our system have been recently addressed within a pseudogap theory [48]. More rigorous treatments could rely on the different many-body  $T$ -matrix theories within the ladder approximation [66, 67].

### Acknowledgments

X.-J.L and H.H. were supported by the ARC Discovery Projects (Grant Nos. FT140100003, FT130100815,

DP140103231 and DP140100637) and the National Key Basic Research Special Foundation of China (NKBRFC-China) (Grant No. 2011CB921502). HP was supported by the NSF, the Welch Foundation (Grant No. C-1669) and the DARPA OLE program.

- 
- [1] I. Bloch, J. Dalibard, and S. Nascimbène, *Nature Phys.* **8**, 267 (2012).
- [2] C. Chin, R. Grimm, P. Julienne, and E. Tiesinga, *Rev. Mod. Phys.* **82**, 1225 (2010).
- [3] Y.-J. Lin, K. Jiménez-García, and I. B. Spielman, *Nature (London)* **471**, 83 (2011).
- [4] M. Z. Hasan and C. L. Kane, *Rev. Mod. Phys.* **82**, 3045 (2010).
- [5] X.-L. Qi and S.-C. Zhang, *Rev. Mod. Phys.* **83**, 1057 (2011).
- [6] D. Xiao, M.-C. Chang, and Q. Niu, *Rev. Mod. Phys.* **82**, 1959 (2010).
- [7] S. -K. Yip, *Annu. Rev. Condens. Matter Phys.* **5**, 15 (2014).
- [8] For a review, see for example, J. Zhang, X.-J. Liu, H. Hu, and H. Pu, *Fermi Gases with Synthetic Spin-Orbit Coupling*. In K. W. Madison, L. D. Carr, and H. Zhai (eds.) *Annual Review of Cold Atoms and Molecules* (volume 2): World Scientific Publishing, chap. 2, pp. 81-143 (2014).
- [9] H. Zhai, arXiv:1403.8021 (2014).
- [10] Y. Xu and C. Zhang, arXiv:1410.3497 (2014).
- [11] J. P. Vyasankere, S. Zhang, and V. B. Shenoy, *Phys. Rev. B* **84**, 014512 (2011).
- [12] S.-L. Zhu, L. B. Shao, Z. D. Wang, and L. M. Duan, *Phys. Rev. Lett.* **106**, 100404 (2011).
- [13] H. Hu, L. Jiang, X.-J. Liu, and H. Pu, *Phys. Rev. Lett.* **107**, 195304 (2011).
- [14] Z.-Q. Yu and H. Zhai, *Phys. Rev. Lett.* **107**, 195305 (2011).
- [15] M. Gong, S. Tewari, and C. Zhang, *Phys. Rev. Lett.* **107**, 195303 (2011).
- [16] L. Jiang, X.-J. Liu, H. Hu, and H. Pu, *Phys. Rev. A* **84**, 063618 (2011).
- [17] X.-J. Liu, L. Jiang, H. Pu, and H. Hu, *Phys. Rev. A* **85**, 021603(R) (2012).
- [18] K. Zhou and Z. Zhang, *Phys. Rev. Lett.* **108**, 025301 (2012).
- [19] L. He and X.-G. Huang, *Phys. Rev. Lett.* **108**, 145302 (2012).
- [20] B. M. Anderson, G. Juzeliūnas, V. M. Galitski, and I. B. Spielman, *Phys. Rev. Lett.* **108**, 235301 (2012).
- [21] M. Gong, G. Chen, S. Jia, and C. Zhang, *Phys. Rev. Lett.* **109**, 105302 (2012).
- [22] K. Seo, L. Han, and C. A. R. Sá de Melo, *Phys. Rev. Lett.* **109**, 105303 (2012).
- [23] X.-J. Liu and H. Hu, *Phys. Rev. A* **85**, 033622 (2012).
- [24] R. Wei and E. J. Mueller, *Phys. Rev. A* **86**, 063604 (2012).
- [25] H. Hu, L. Jiang, H. Pu, Y. Chen, and X.-J. Liu, *Phys. Rev. Lett.* **110**, 020401 (2013).
- [26] L. He and X.-G. Huang, *Ann. Phys. (N.Y.)* **337**, 163 (2013).
- [27] Z. Zheng, M. Gong, X. Zou, C. Zhang, and G.-C. Guo, *Phys. Rev. A* **87**, 031602(R) (2013).
- [28] L. Dong, L. Jiang, H. Hu, and H. Pu, *Phys. Rev. A* **87**, 043616 (2013).
- [29] F. Wu, G.-C. Guo, W. Zhang, and W. Yi, *Phys. Rev. Lett.* **110**, 110401 (2013).
- [30] X.-J. Liu and H. Hu, *Phys. Rev. A* **87**, 051608(R) (2013).
- [31] L. Dong, L. Jiang, and H. Pu, *New J. Phys.* **15**, 075014 (2013).
- [32] X.-F. Zhou, G.-C. Guo, W. Zhang, and W. Yi, *Phys. Rev. A* **87**, 063606 (2013).
- [33] H. Hu and X.-J. Liu, *New J. Phys.* **15**, 093037 (2013).
- [34] K. Seo, C. Zhang, and S. Tewari, *Phys. Rev. A* **87**, 063618 (2013).
- [35] M. Iskin, *Phys. Rev. A* **88**, 013631 (2013).
- [36] B. M. Anderson, I. B. Spielman, and G. Juzeliūnas, *Phys. Rev. Lett.* **111**, 125301 (2013).
- [37] C. Chen, *Phys. Rev. Lett.* **111**, 235302 (2013).
- [38] X.-J. Liu and H. Hu, *Phys. Rev. A* **88**, 023622 (2013).
- [39] C. Qu, Z. Zheng, M. Gong, Y. Xu, L. Mao, X. Zou, G. Guo, and C. Zhang, *Nat. Comm.* **4**, 2710 (2013).
- [40] W. Zhang and W. Yi, *Nat. Comm.* **4**, 2711 (2013).
- [41] V. B. Shenoy, *Phys. Rev. A* **88**, 033609 (2013).
- [42] X.-J. Liu, *Phys. Rev. A* **88**, 043607 (2013).
- [43] H. Hu, L. Dong, Y. Cao, H. Pu, and X.-J. Liu, *Phys. Rev. A* **90**, 033624 (2014).
- [44] Y. Xu, R. Chu, and C. Zhang, *Phys. Rev. Lett.* **112**, 136402 (2014).
- [45] Y. Cao, S.-H. Zou, X.-J. Liu, S. Yi, G.-L. Long, and H. Hu, *Phys. Rev. Lett.* **113**, 115302 (2014).
- [46] J. P. A. Devreese, J. Tempere, and C. A. R. Sá de Melo, *Phys. Rev. Lett.* **113**, 165304 (2014).
- [47] L. Jiang, E. Tiesinga, X.-J. Liu, H. Hu, and H. Pu, *Phys. Rev. A* **90**, 053606 (2014).

- [48] Z. Zheng, H. Pu, X. Zou, and G.-C. Guo, arXiv:1407.3203 (2014).
- [49] Y. Cao, X.-J. Liu, L. He, G.-L. Long, and H. Hu, arXiv:1410.0987 (2014).
- [50] P. Wang, Z.-Q. Yu, Z. Fu, J. Miao, L. Huang, S. Chai, H. Zhai, and J. Zhang, Phys. Rev. Lett. **109**, 095301 (2012).
- [51] L. W. Cheuk, A. T. Sommer, Z. Hadzibabic, T. Yefsah, W. S. Bakr, and M. W. Zwierlein, Phys. Rev. Lett. **109**, 095302 (2012).
- [52] R. A. Williams, M. C. Beeler, L. J. LeBlanc, K. Jiménez-García, and I. B. Spielman, Phys. Rev. Lett. **111**, 095301 (2013).
- [53] Z. Fu, L. Huang, Z. Meng, P. Wang, X.-J. Liu, H. Pu, H. Hu, and J. Zhang, Phys. Rev. A **87**, 053619 (2013).
- [54] F. Wilczek, Nature Phys. **5**, 614 (2009).
- [55] J. D. Sau and S. Tewari, Phys. Rev. B **86**, 104509 (2012).
- [56] P. Fulde and R. A. Ferrell, Phys. Rev. **135**, A550 (1964).
- [57] S. Giorgini, L. P. Pitaevskii, and S. Stringari, Rev. Mod. Phys. **80**, 1215 (2008).
- [58] V. Barzykin and L. P. Gor'kov, Phys. Rev. Lett. **89**, 227002 (2002).
- [59] S. K. Yip, Phys. Rev. B **65**, 144508 (2002).
- [60] D. F. Agterberg and R. P. Kaur, Phys. Rev. B **75**, 064511 (2007).
- [61] O. Dimitrova and M. V. Feigel'man, Phys. Rev. B **76**, 014522 (2007).
- [62] K. Michaeli, A. C. Potter, and P. A. Lee, Phys. Rev. Lett. **108**, 117003 (2012).
- [63] C. L. M. Wong, J. Liu, K. T. Law, and P. A. Lee, Phys. Rev. B **88**, 060504(R) (2013).
- [64] This is a branch cut at  $k_z = 0$  to a 3D surface plot of the energy spectrum, as shown, for example, in Figs. 2(b) and 2(c).
- [65] M. J. H. Ku, A. T. Sommer, L. W. Cheuk, and M. W. Zwierlein, Science **335**, 563 (2012).
- [66] H. Hu, X.-J. Liu, and P. D. Drummond, Europhys. Lett. **74**, 574 (2006).
- [67] H. Hu, X.-J. Liu, and P. D. Drummond, Phys. Rev. A **77**, 061605 (2008).